*remote sensing*

MDPI

*Article*

# Inter-Comparison of SST Products from iQuam, AMSR2/GCOM-W1, and MWRI/FY-3D

**Yili Zhao [1,*], Ping Liu [1] and Wu Zhou [2]**

[1] School of Marine Technology and Geomatics, Jiangsu Ocean University, Lianyungang 222005, China; lp@jou.edu.cn
[2] National Satellite Ocean Application Service, Beijing 100081, China; zhouwu@mail.nsoas.org.cn
* Correspondence: yili.zhao@jou.edu.cn

**Abstract:** Evaluating sea surface temperature (SST) products is essential before their application in marine environmental monitoring and related studies. SSTs from the in situ SST Quality Monitor (iQuam) system, Advanced Microwave Scanning Radiometer 2 (AMSR2) aboard the Global Change Observation Mission 1st-Water, and the Microwave Radiation Imager (MWRI) aboard the Chinese Fengyun-3D satellite are intercompared utilizing extended triple collocation (ETC) and direct comparison methods. Additionally, error characteristic variations with respect to time, latitude, SST, sea surface wind speed, columnar water vapor, and columnar cloud liquid water are analyzed comprehensively. In contrast to the prevailing focus on SST validation accuracy, the random errors and the capability to detect SST variations are also evaluated in this study. The result of ETC analysis indicates that iQuam SST from ships exhibits the highest random error, above 0.83 °C, whereas tropical mooring SST displays the lowest random error, below 0.28 °C. SST measurements from drifters, tropical moorings, Argo floats, and high-resolution drifters, which possess random errors of less than 0.35 °C, are recommended for validating remotely sensed SST. The ability of iQuam, AMSR2, and MWRI to detect SST variations diminishes significantly in ocean areas between 0°N and 20°N latitude and latitudes greater than 50°N and 50°S. AMSR2 and iQuam demonstrate similar random errors and capabilities for detecting SST variations, whereas MWRI shows a high random error and weak capability. In comparison to iQuam SST, AMSR2 exhibits a root-mean-square error (RMSE) of about 0.51 °C with a bias of −0.05 °C, while MWRI shows an RMSE of about 1.26 °C with a bias of −0.14 °C.

**Keywords:** sea surface temperature; validation; AMSR2; MWRI; iQuam; extended triple collocation

check for updates

**Citation:** Zhao, Y.; Liu, P.; Zhou, W. Inter-Comparison of SST Products from iQuam, AMSR2/GCOM-W1, and MWRI/FY-3D. *Remote Sens.* **2024**, *16*, 2034. https://doi.org/10.3390/rs16112034

Academic Editors: Jorge Vazquez and Eileen Maturi

Received: 29 April 2024
Revised: 25 May 2024
Accepted: 4 June 2024
Published: 6 June 2024

**Copyright:** © 2024 by the authors. Licensee MDPI, Basel, Switzerland. This article is an open access article distributed under the terms and conditions of the Creative Commons Attribution (CC BY) license (https://creativecommons.org/licenses/by/4.0/).

## 1. Introduction

Sea surface temperature (SST) serves as a fundamental variable for monitoring, understanding, and predicting the fluxes of heat, momentum and gases across various scales, which govern the intricate interplay between the atmosphere and the ocean [1–5]. SST patterns exhibit close associations with subsurface dynamics, including fronts and eddies [6–8]. Alterations in SST patterns offer valuable insights into large-scale disruptions to global circulation and multi-decadal climate changes [9–11]. Continuous monitoring of the spatial and temporal distributions of SST is indispensable for advancing the understanding of the mechanisms and impacts associated with SST variations.

In situ SST measurements can extend back over 160 years [12]. Traditionally, these measurements were collected from moored buoys, drifting buoys, and ships [13]. However, these sources of data suffer from temporal and spatial discontinuities. In contrast, satellite-based sensors including infrared radiometers and microwave radiometers provide an optimal method for global ocean SST observations [14]. In the infrared band, sea temperature can be observed with a spatial resolution of a few kilometers and an accuracy ranging from 0.3 to 0.6 °C [15–17]. However, infrared radiometers cannot observe SST

under cloudy conditions, which restricts their application in global SST monitoring. In contrast, microwave radiometers operate in the microwave band with longer electromagnetic wave wavelengths, allows them to penetrate through clouds and rain, enabling the observation of SST in all weather conditions [18].

Since 1978, with the launch of the Multichannel Microwave Radiometer (SMMR) onboard the SEASAT spacecraft, satellite-based microwave radiometers have facilitated global SST observations for several decades [14,19]. Compared with ship observation, SST accuracy derived from SMMR is 0.75 °C due to inadequate calibration [20]. The launch of the Tropical Rainfall Measuring Mission Microwave Imager (TMI) facilitated the acquisition of high-quality microwave SST data. Compared with Reynolds and Smith SST analysis and in situ measurements, TMI SST products were shown have a standard deviation below 0.6 °C [21,22]. Since then, satellite-based microwave radiometers, such as the Advanced Microwave Scanning Radiometer-Earth Observing System (AMSR-E), WindSat, Advanced Microwave Scanning Radiometer 2 (AMSR2), and Global Precipitation Measurement Microwave Imager (GMI), have significantly contributed to global SST observations. The accuracy of SST products derived from these satellite-based microwave radiometers has been demonstrated to fall within the range of 0.4~0.6 °C [23–26]. Scanning microwave radiometers aboard Chinese marine dynamic environment satellites Haiyang 2A (HY-2A) and HY-2B were launched in 2011 and 2018, respectively. Compared to global in situ measurements from mooring and Argo buoys, the root-mean-square error (RMSE) of the SST product derived from the scanning microwave radiometer onboard HY-2A is approximately 1.7 °C [27,28]. Following updates to the design of the cold space antenna, sensor calibration, and retrieval algorithm, the RMSE of SST observations from the scanning microwave radiometer onboard HY-2B was reduced to 1.06 °C [29]. The Chinese Fengyun-3 (FY-3) series of meteorological satellites, including FY-3 A, B, C, and D also equipped with the Microwave Radiation Imager (MWRI), which were launched in 2008, 2010, 2013, and 2017, respectively. Compared to global buoy measurements, FY-3C MWRI SST exhibits a standard deviation of 1.22 K and 1.28 K for ascending and descending orbits, respectively [30].

In this study, the accuracies of SST products from MWRI onboard FY-3D, AMSR2 onboard the Global Change Observation Mission 1st-Water (GCOM-W1), and in situ SST Quality Monitor (iQuam) are evaluated using extend triple collocation (ETC) and direct comparison methods. Additionally, their capability to detect SST variation is also evaluated. The dataset and methods are described in Section 2, and the validation results and discussion are presented in Sections 3 and 4, respectively. Section 5 provides a summary.

## 2. Materials and Methods

### *2.1. Data*

#### 2.1.1. MWRI SST

The MWRI is a primary sensor onboard the FY-3D satellite, operating at frequencies of 10.65, 18.7, 23.8, 36.5, and 89 GHz. It conducts dual-polarized (vertical and horizontal) observations at all frequencies [31]. Table 1 presents the instrument parameters of the MWRI. The FY-3D satellite operates on a sun-synchronous orbit with a Local Time of the Ascending Node (LTAN) at 14:00. This configuration implies that observations in the ascending orbit occur during the daytime, while those in the descending orbit occur during the nighttime.

**Table 1.** Instrument parameters of MWRI.

| Frequency (GHz) | Polarization | Band Width (MHz) | IFOV (km) | NEΔT (k) |
|---|---|---|---|---|
| 10.65 | V.H | 180 | 51 × 85 | 0.5 |
| 18.7 | V.H | 200 | 30 × 50 | 0.5 |
| 23.8 | V.H | 400 | 27 × 45 | 0.5 |
| 36.5 | V.H | 900 | 18 × 30 | 0.5 |
| 89 | V.H | 2 × 2300 | 9 × 15 | 0.8 |

The SST product of FY-3 MWRI was generated using a multi-channel linear regression method [30]. This paper evaluates the Level 2 orbital SST product provided by the National Satellite Meteorological Center. All Level 2 SST products from 30 April 2019 to 31 December 2023 were collected in February 2024 from the National Satellite Meteorological Center website. Approximately 28 Level 2 orbital SST data files are available each day. Each data file contains observations from a single pass and provides scientific parameters including longitude, latitude, scanning line time, sea surface temperature, rain status, sea ice status, and data quality markers. Quality indicators for the SST product are defined as follows for these parameters: 1 denotes invalid observation pixels, 2 denotes precipitation pixels, 3 denotes sea ice pixels, 4 denotes estimated SST values outside the range of 271.15–308.15 K, 50 represents the difference between estimated SST values and monthly mean SST values less than 2.5 K, and 51 represents the difference between estimated SST values and monthly mean SST values greater than 2.5 K.

#### 2.1.2. AMSR2 SST

The AMSR2 onboard the GCOM-W1 satellite was launched on 18 May 2012 [32]. GCOM-W1 operates in a sun-synchronous orbit with the LTAN at 13:30 ± 15, similar to FY-3D. This enhances the likelihood of matching SST observations between AMSR2 and MWRI. AMSR2 operates in seven channels: 6.93, 7.3, 10.65, 18.7, 23.8, 36.5, and 89 GHz, with both horizontal and vertical polarizations. Notably, AMSR2 includes an additional frequency of 7.3 GHz to mitigate radio frequency interference, distinguishing it from other spaceborne microwave radiometers [32]. Table 2 presents the instrument parameters of AMSR2.

**Table 2.** Instrument parameters of AMSR2.

| Frequency (GHz) | Polarization | Band Width (MHz) | IFOV (km) | NEΔT (k) |
|---|---|---|---|---|
| 6.925 | V.H | 350 | 35 × 62 | <0.34 |
| 7.3 | V.H | 350 | 35 × 62 | <0.43 |
| 10.65 | V.H | 100 | 24 × 42 | <0.70 |
| 18.7 | V.H | 200 | 14 × 22 | <0.70 |
| 23.8 | V.H | 400 | 15 × 26 | <0.60 |
| 36.5 | V.H | 1000 | 7 × 12 | <0.70 |
| 89 | V.H | 3000 | 3 × 5 | <1.20/1.40[2] |

The AMSR2 daily product, version 8.2, generated by the Remote Sensing Systems (RSS), is evaluated in this study. The daily product files consist of seven parameters: time (UTC), SST, 10 m surface wind speed, atmospheric water vapor, cloud liquid water, and rain rate. All parameters are mapped onto a 0.25° grid, which is further divided into two maps based on ascending and descending passes.

#### 2.1.3. iQuam SST

In situ SST measurements are commonly used as the standard "ground truth" for calibrating and validating satellite SST retrievals. However, the quality of in situ measurements varies depending on the platforms, sensors, agencies, and manufacturers involved [33]. To meet the demands of satellite calibration and validation using in situ data, which require

flexible and scalable quality control, the National Oceanic and Atmospheric Administration (NOAA) developed a near real-time in situ SST Quality Monitor system (iQuam). iQuam conducts advanced, flexible, and unified community consensus quality control for in situ SST data, including duplicate removal, plausibility checks, platform tracking, SST spike checking and reference and cross-platform verification [13].

This study uses iQuam version v2.1, which includes in situ SST measurements from various platforms, such as conventional ships, drifters, tropical moorings (T-M), coastal moorings (C-M), Argo floats, high-resolution drifters (HR-D), Integrated Marine Observing System (IMOS) ships, and Coral Reef Watch (CRW) coastal buoys.

### *2.2. Method*

#### 2.2.1. Quality Control

Utilizing the quality flag associated with MWRI Level 2 SST product, pixels with precipitation, sea ice, and anomalous temperature inversion data are initially filtered out. Following the suggestion from Zhang et al. (2018), MWRI SST with a quality flag of 51 is excluded from this study [30]. Pixels with a quality flag of 51 account for 21% of the total. All the SSTs from MWRI and AMSR2 with an off-shore distance of less than 50 km are excluded, filtering the SST retrievals with land contamination.

iQuam SSTs with a quality level of 5, recommended for high-precision applications, are selected for SST comparison in this study. To minimize discrepancies in sea water temperature caused by different depths, iQuam SSTs with a measuring depth greater than 5 m are excluded.

#### 2.2.2. Data Collocation

SSTs collected from MWRI, AMSR2, and iQuam span from 30 April 2019 to 31 December 2023. Initially, spatiotemporal matching is performed between MWRI SST and iQuam SST, followed by matching the results with AMSR2 SST to create triple-collocations. During the matching process, the spatial distance constraint between observations is set at 25 km, and the time difference limit is 30 min. Considering the differences in the performance of in situ measuring platforms and buoy types, the collocations are stratified into ships, drifters, T-M, C-M, Argo, HR-D, and IMOS. Figure 1 exhibits the spatial distribution of the collocations. To avoid interference from diurnal variations in SST during intercomparison, the collocations are divided into daytime and nighttime groups. Table 3 lists the number of collocations.

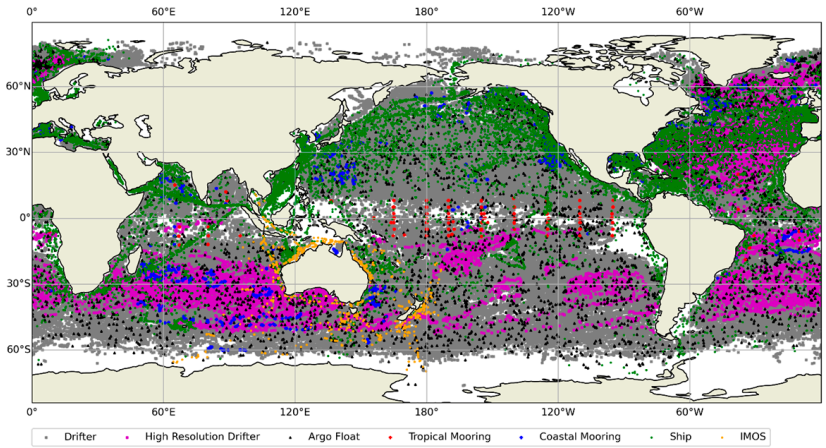


**Figure 1.** Spatial distribution of triple collocations.

**Table 3.** Counts of collocations.

| Observation Time | iQuam Platforms | | | | | | | |
|---|---|---|---|---|---|---|---|---|
| | **ALL** | **Ship** | **Drifting** | **T-M** | **C-M** | **Argo** | **HR-D** | **IMOS** |
| Daytime | 279,246 | 14,534 | 171,704 | 3194 | 67,499 | 2001 | 12,655 | 7625 |
| Nighttime | 268,786 | 11,702 | 171,578 | 3516 | 57,092 | 2318 | 13,244 | 9301 |

#### 2.2.3. Comparison Method

Compared SST observations from infrared or microwave radiometers with in situ SST measurements from moored buoys, drifting buoys, and ship-based buoys is a common method for assessing the accuracy of remotely sensed SST [21,26,27,29,34]. This method assumes that the in situ data represent the ground truth. However, in situ SST measurements suffer from observational random and systematic observational errors, leading to biases and uncertainties that cannot be neglected in high-precision applications [12,35]. Additionally, in situ SST, which represents the temperature free of diurnal temperature variability, is akin to foundation SST. In situ SST is typically measured by temperature sensors mounted on various buoys and ships at depths of 1–5 m, whereas remote sensors observe the water temperature at a shallow depth near the ocean surface [36,37]. Infrared radiometers measure skin SST at a depth on the order of 0.01 mm, depending on the wavelength of the measurement [37,38]. Microwave radiometers measure subskin SST, representing the temperature at the bottom of the skin SST gradient at a depth of approximately 1 mm, corresponding to the attenuation length of microwave radiation [37]. Two processes, the cool-skin and diurnal warming effects, cause significant differences among the skin, subskin, and foundation SSTs [39,40]. These differences introduce errors in validating remotely sensed SST when using in situ SST as a single reference. To overcome the limitations of direct comparison methods and generate more reliable validation results, a triple collocation (TC) method was developed [41]. TC is a methodology for estimating the random error variances of three mutually independent measurement systems when there is no known "truth" [41,42]. TC has been widely used for validating soil moisture [43–45], precipitation [46,47], sea surface salinity [48], SST [49], sea surface wind, and waves [41,50]. Based on TC, extended triple collocation (ETC) was proposed. ETC utilizes the same assumptions as TC but derives additional performance metrics, including the correlation coefficient of the measurement system with respect to the unknown target and the scaled, unbiased signal-to-noise ratio. ETC provides a complementary perspective compared to the error standard deviation [51]. However, TC or ETC should not substitute the direct comparison method because they estimate limited product errors [42]. A single method can never capture all the relevant characteristics of the relationship between the measurement system and the target, including the measurement system's bias, noise, RMSE, and sensitivity with respect to the target variable [52].

SST measurement validation primarily aims to estimate the absolute accuracy of the observations. However, it is also essential to evaluate the sensitivity of the SST measurement system to local or larger-scale spatial variability and temporal changes, such as diurnal warming and cooling. In this study, both ETC and direct comparison methods are utilized to intercompare SSTs from MWRI, AMSR2, and iQuam. ETC is used to estimate the independent random errors of the three SST measurement systems and their abilities for SST variation detection. The direct comparison method is employed to calculate the systemic bias and RMSE of MWRI SST and AMSR2 SST relative to iQuam SST. Additionally, variations in errors with respect to time, latitude, SST, sea surface wind, columnar water vapor, and columnar cloud liquid water are analyzed to deepen the understanding of the errors.

(a) Extend triple collocation

The most commonly used error model for TC analysis can be expressed as follows:

$$X_i = \alpha_i + \beta_i T + \varepsilon_i \tag{1}$$

where $X_i (i \in \{1, 2, 3\})$ represents collocated measurements from three independent measurement systems, linearly related to the unknown truth value T. $\alpha_i$ and $\beta_i$ represent the systematic additive and multiplicative biases of measurement i relative to the truth, while $\varepsilon_i$ represents random noise. The underlying assumptions for the error model are as follows: (i) the triple measurements are entirely independent of each other (zero cross-correlation assumption); (ii) the errors of the three measurement systems are independent of each other and unrelated to other products as long as the truth value is known (error orthogonality); and (iii) the expected values of the errors are zero (zero error expectation) [53].

The covariances between the different measurement systems are given by

$$Q_{ij} = \mathrm{Cov}(X_i, X_j) = E(X_i X_j) - E(X_i)E(X_j) = \beta_i \beta_j \sigma_T^2 + \beta_j \mathrm{Cov}(T, \varepsilon_i) + \beta_i \mathrm{Cov}(T, \varepsilon_j) + \mathrm{Cov}(\varepsilon_i, \varepsilon_j) \tag{2}$$

$$\sigma_T^2 = \mathrm{Var}(T) \tag{3}$$

Based on the assumptions ii and iii, we have $\mathrm{Cov}(T, \varepsilon_i) = 0, \mathrm{Cov}(T, \varepsilon_j) = 0, \mathrm{Cov}(\varepsilon_i, \varepsilon_j) = 0$, and $E(\varepsilon_i) = 0$. So, Equation (4) can be reduced to

$$Q_{ij} = \begin{cases} \beta_i \beta_j \sigma_T^2 & \text{for } i \neq j \\ \beta_i^2 \sigma_T^2 + \sigma_{\epsilon_i}^2 & \text{for } i = j \end{cases} \tag{4}$$

where $\sigma_{\varepsilon_i}^2 = \mathrm{Var}(\varepsilon_i)$. If we define a new variable $\theta_i = \beta_i \varepsilon_T$, then Equation (5) can be written as

$$Q_{ij} = \begin{cases} \theta_i \theta_j & \text{for } i \neq j \\ \theta_i^2 + \sigma_{\varepsilon_i}^2 & \text{for } i = j \end{cases} \tag{5}$$

The error standard deviations (ESD) of the three measurement systems can be obtained by solving six equations ($Q_{11}$, $Q_{12}$, $Q_{13}$, $Q_{22}$, $Q_{23}$, $Q_{33}$) with six unknown variables ($\theta_1$, $\theta_2$, $\theta_3$, $\sigma_{\varepsilon_1}$, $\sigma_{\varepsilon_2}$, $\sigma_{\varepsilon_3}$).

$$\sigma_{\varepsilon i} = \begin{bmatrix} \sqrt{Q_{11} - \frac{Q_{12}Q_{13}}{Q_{23}}} \\ \sqrt{Q_{22} - \frac{Q_{12}Q_{23}}{Q_{13}}} \\ \sqrt{Q_{33} - \frac{Q_{13}Q_{23}}{Q_{12}}} \end{bmatrix} \tag{6}$$

Beyond $\sigma_\varepsilon$, ETC [51] obtains the correlation coefficient between T and $X_i$,

$$\rho_{T,X_i} = \pm \begin{bmatrix} \sqrt{\frac{Q_{12}Q_{13}}{Q_{11}Q_{23}}} \\ \mathrm{sign}(Q_{13}Q_{23}) \sqrt{\frac{Q_{12}Q_{23}}{Q_{22}Q_{13}}} \\ \mathrm{sign}(Q_{12}Q_{23}) \sqrt{\frac{Q_{13}Q_{23}}{Q_{33}Q_{12}}} \end{bmatrix} \tag{7}$$

where $\rho_{t,X_i}$ represents the correlation coefficient. Moreover, the scaled unbiased signal-to-noise ratio $SNR_{SUb}$ is defined as follows [51].

$$SNR_{Sub} = \rho_{T,X_i}^2 = \frac{\beta_i^2 \sigma_T^2}{\beta_i^2 \sigma_T^2 + \sigma_{\varepsilon_i}^2} = \frac{SNR_{ub}}{SNR_{ub}+1} \tag{8}$$

where $SNR_{ub} = \frac{\beta_i^2 \sigma_t^2}{\sigma_{\varepsilon_i}^2}$ is unbiased signal-to-noise-ratio. $SNR_{SUb}$ contains the information about the sensitivity of the measurement system and can be used to evaluate the noise level of the measurement system if found suitable for detecting the signal of the variation in the target variable [51]. In this study, $SNR_{SUb}$ was employed as an indicator for the ability of the measurement system to detect SST variations.

(b) Direct comparison

The bias and RMSE of MWRI SST and AMSR2 SST relative to iQuam SST are calculated using the direct comparison method. These two parameters are defined as follows.

$$\text{Bias} = \frac{\sum_{i=0}^{n}(\text{SST}_{\text{RS,i}} - \text{SST}_{\text{iQuam,i}})}{n} \quad (9)$$

$$\text{RMSE} = \sqrt{\frac{\sum_{i=0}^{n}(\text{SST}_{\text{RS,i}} - \text{SST}_{\text{iQuam,i}})^2}{n}} \quad (10)$$

where $\text{SST}_{\text{RS}}$ represents the SST observed by MWRI or AMSR2, and $\text{SST}_{\text{iQuam}}$ represents the SST measurements of iQuam.

## 3. Results

### *3.1. ETC Analysis*

ETC is utilized to assess the performance of three independent SST measurement systems. ESD represents the random error of the measurement system, while $\text{SNR}_{\text{SUb}}$ indicates the system's ability to detect variations in SST. Tables 4 and 5 present the ESD and $\text{SNR}_{\text{SUb}}$ values of iQuam, AMSR2, and MWRI during daytime and nighttime, respectively. iQuam exhibits a total ESD of 0.41 °C during the day and 0.38 °C at night, with $\text{SNR}_{\text{SUb}}$ values being closely matched between the two periods. Comparing the performance of iQuam SST across different platforms reveals that ships consistently exhibit higher random errors than other platforms. Drifters and HR-D, being of the same platform type, share identical ESD values during both daytime and nighttime, yet the differences in their spatial distributions lead to distinct $\text{SNR}_{\text{SUb}}$ values. Argo demonstrates nearly identical performance to Drifters. T-M exhibits the lowest random error during both daytime and nighttime, but its minimum $\text{SNR}_{\text{SUb}}$ values suggest inadequate noise levels for detecting full tropical SST variations. Both T-M and C-M show higher random errors during the day than at night, possibly due to diurnal warming effects causing SST differences at varying depths. Compared to T-M, C-M displays greater random error, yet higher $\text{SNR}_{\text{SUb}}$ values indicate that the noise level of C-M is acceptable for detecting coastal SST variation. During the day, AMSR2 records a total ESD of 0.43 °C and $\text{SNR}_{\text{SUb}}$ of 0.9972. AMSR2's total ESD at night is slightly lower, while that of $\text{SNR}_{\text{SUb}}$ is slightly higher, indicating better nighttime performance. MWRI exhibits similar characteristics but with a higher ESD and lower $\text{SNR}_{\text{SUb}}$ Due to differences in the spatial distribution of the iQuam platform (illustrated in Figure 1), the results of both AMSR2 and MWRI SST ETC analyses vary with the iQuam platform.

**Table 4.** Results of ETC analysis during daytime.

| Data | ETC Results | ALL | Ship | Drifting | T-M | C-M | Argo | HR-D | IMOS |
|---|---|---|---|---|---|---|---|---|---|
| iQuam | ESD °C | 0.41 | 0.83 | 0.30 | 0.28 | 0.51 | 0.32 | 0.30 | 0.52 |
| | $\text{SNR}_{SUb}$ | 0.9976 | 0.9892 | 0.9986 | 0.9852 | 0.9962 | 0.9988 | 0.9979 | 0.9962 |
| AMSR2 | ESD °C | 0.43 | 0.65 | 0.42 | 0.15 | 0.38 | 0.45 | 0.38 | 0.31 |
| | $\text{SNR}_{SUb}$ | 0.9972 | 0.9935 | 0.9974 | 0.9962 | 0.9979 | 0.9976 | 0.9966 | 0.9987 |
| MWRI | ESD °C | 1.22 | 1.27 | 1.21 | 0.89 | 1.21 | 1.22 | 1.21 | 1.17 |
| | $\text{SNR}_{SUb}$ | 0.9775 | 0.9752 | 0.9777 | 0.8640 | 0.9778 | 0.9817 | 0.9637 | 0.9806 |

**Table 5.** Results of ETC analysis during nighttime.

| Data | ETC Results | ALL | Ship | Drifting | T-M | C-M | Argo | HR-D | IMOS |
|---|---|---|---|---|---|---|---|---|---|
| iQuam | ESD °C | 0.38 | 0.84 | 0.32 | 0.20 | 0.41 | 0.35 | 0.32 | 0.54 |
| | $SNR_{SUb}$ | 0.9978 | 0.9896 | 0.9985 | 0.9913 | 0.9976 | 0.9985 | 0.9975 | 0.9960 |
| AMSR2 | ESD °C | 0.41 | 0.58 | 0.39 | 0.21 | 0.42 | 0.34 | 0.36 | 0.44 |
| | $SNR_{SUb}$ | 0.9975 | 0.9952 | 0.9976 | 0.9913 | 0.9975 | 0.9986 | 0.9969 | 0.9975 |
| MWRI | ESD °C | 1.19 | 1.17 | 1.18 | 0.97 | 1.13 | 1.20 | 1.17 | 1.15 |
| | $SNR_{SUb}$ | 0.9788 | 0.9799 | 0.9787 | 0.8016 | 0.9810 | 0.9823 | 0.9666 | 0.9828 |

### *3.2. Direct Comparison*

The systemic bias and RMSE of SST observations from AMSR2 and MWRI are estimated through direct comparison with SST measurements from iQuam serving as the ground truth. These parameters bolster confidence in the operational application of remotely sensed SST and provide crucial insights for enhancing retrieval algorithms. It is noteworthy that, considering the random error assessed by ETC analyses (listed in Tables 4 and 5) and the spatial distribution of each iQuam platform, only SST measurements from Drifter, T-M, Argo, and HR-D are chosen for direct comparison in this section and error analyses in Section 3.2. Figure 2 illustrates density plots of AMSR2 SST ($y$-axis) versus iQuam SST ($x$-axis). Compared to iQuam SST, AMSR2 SST exhibits a total bias of −0.04 °C and an RMSE of 0.52 °C during daytime and a bias of −0.05 °C and an RMSE of 0.50 °C during nighttime. Similarly, Figure 3 presents the SST comparison between MWRI and iQuam. The total bias and RMSE of MWRI SST during daytime are −0.33 °C and 1.30 °C, respectively, while during nighttime, they are 0.05 °C and 1.22 °C. It can be inferred that both AMSR2 and MWRI perform better at night than during the day, aligning with the findings of the ETC analyses.

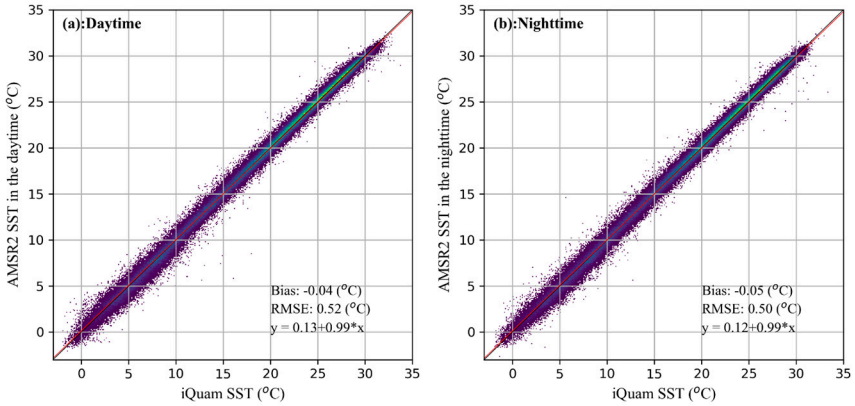


**Figure 2.** Comparison between AMSR2 SST and iQuam SST in the daytime and nighttime. (**a**) Daytime. (**b**) Nighttime.

The results of the ETC analyses indicate that the performances of AMSR2 and MWRI vary depending on the location. To comprehensively assess the performance of SST measurements from AMSR2 and MWRI across the global ocean, the spatial distributions of SST bias relative to iQuam are examined. Figure 4 illustrates the mean difference between AMSR2 SST and iQuam SST in geogrids with a spatial resolution of 1° during both daytime and nighttime. As depicted in Figure 4a, AMSR2 SST during the daytime exhibits the warmest bias in oceanic regions with latitudes greater than 60°, with a maximum bias value of approximately 0.8 °C. The abnormal warm bias of AMSR2 SST in the Arctic Ocean may be attributed to ice contamination, along with the robustness of the retrieval algorithm in cold water. In the northeast Pacific, tropical ocean, and coastal areas, AMSR2 SST during

the daytime shows a warm bias ranging from 0.25 °C to 0.5 °C, while bias in the open ocean ranges from −0.25 °C to 0.25 °C. The spatial distribution of bias for AMSR2 SST during nighttime (Figure 4b) exhibits similarities. Compared to daytime bias, nighttime bias for AMSR2 SST shows a warmer trend in the Southern Ocean and areas affected by the Kuroshio and North Pacific currents, while the warm bias in the northeast Pacific weakens.

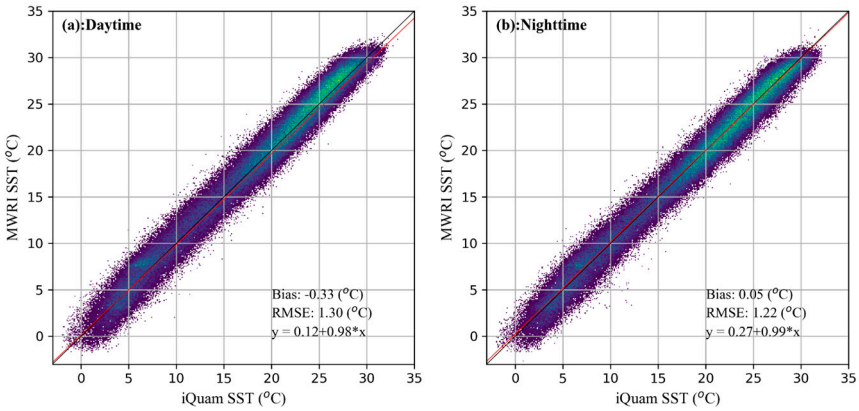


**Figure 3.** Comparison between MWRI SST and iQuam SST in the daytime and nighttime. (**a**) Daytime. (**b**) Nighttime.

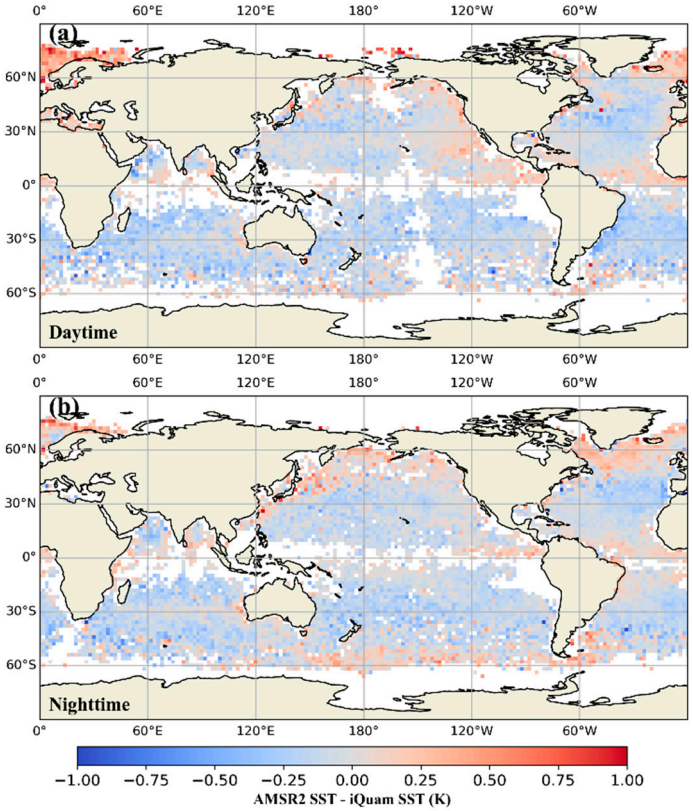


**Figure 4.** Spatial distribution of AMSR2 SST bias referring to iQuam SST. (**a**) Daytime. (**b**) Nighttime.

It should be noted that the warm bias of AMSR2 SST relative to iQuam SST in coastal areas is likely due to representativeness differences rather than errors in AMSR2 SST. The footprint size of AMSR2 at 6.925 GHz is 35 × 62 km, which is the primary channel for SST retrieval, indicating that AMSR2 SST closely represents the mean SST over this footprint. In contrast, iQuam SST represents a point measurement. When SST variation within the footprint is significant, the representativeness difference results in discrepancies between AMSR2 and iQuam SSTs. Coastal areas typically exhibit significant SST variations, which

highlight the representativeness difference. This situation also occurs in regions with significant SST gradients, such as those affected by the Kuroshio current.

Figure 5 illustrates the spatial distribution of MWRI bias relative to iQuam SST during both daytime and nighttime. Compared to AMSR2 SST, MWRI SST exhibits greater bias variation and distinct spatial distributions. During the daytime, MWRI SST shows warmer bias in oceanic regions with latitudes lower than −30°, while most areas with latitudes greater than −30° exhibit negative biases. As depicted in Figure 5b, MWRI SST during nighttime displays warm bias across most oceanic regions in the Southern Hemisphere, with a maximum bias of approximately 2.0 °C. In the northern Pacific and northern Atlantic, MWRI SST during nighttime exhibits biases ranging from 0 to 0.5 °C.

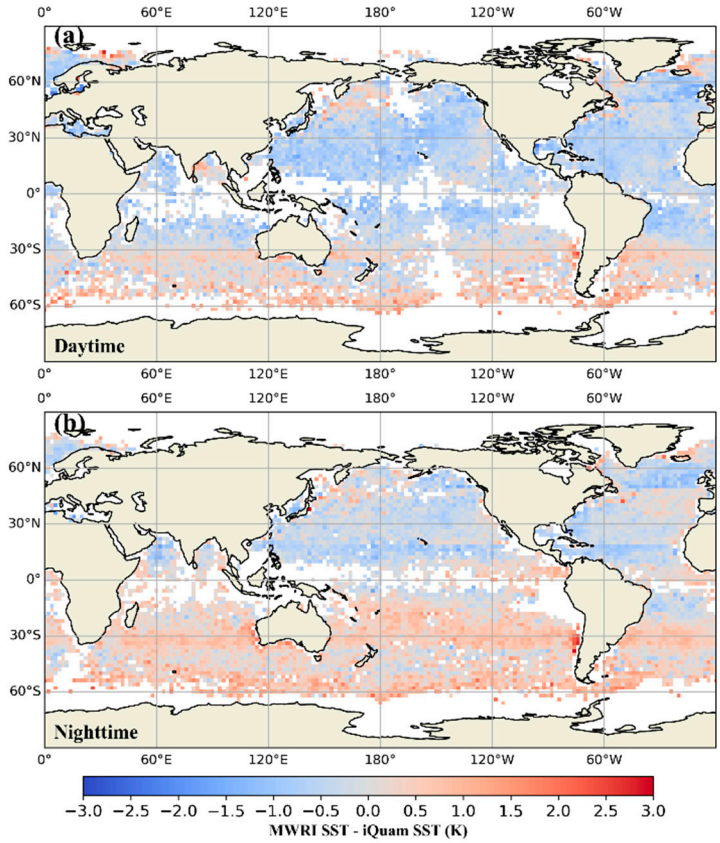


**Figure 5.** Spatial distribution of SST difference between MWRI and iQuam. (**a**) Daytime. (**b**) Nighttime.

### *3.3. Error Analyses*

To mitigate spurious signals in SST variation, all the SST measurement systems are expected to have uniform performance across time and location. The SST observations from satellite-based microwave radiometers are susceptible to crosstalk effects from sea surface wind, water vapor, and cloud liquid water, as documented in prior studies [54,55]. In light of these considerations, variations in the ESD and $SNR_{SUb}$ of AMSR2, MWRI, and iQuam are examined with respect to time, latitude, SST, sea surface wind, columnar water vapor, and columnar cloud liquid water. Additionally, variations in bias and RMSE of AMSR2 and MWRI SST, relative to iQuam SST, are concurrently analyzed.

(a) Temporal variation in error characteristics

Figure 6 depicts the temporal variation in error characteristics. Monthly and global collocations are extracted to calculate the error characteristics. From April 2019 to December 2023, all error characteristics of AMSR2 and iQuam SST demonstrate temporal stability, with daytime and nighttime curves nearly overlapping. During July 2019 to March 2022, iQuam SST exhibits lower ESD and higher $SNR_{SUb}$ compared to AMSR2, indicating reduced

random error and increased sensitivity to SST variation. However, from April 2019 to June 2019 and from April 2022 to December 2023, distinguishing between the ESD and $SNR_{SUb}$ of AMSR2 and iQuam proves challenging. In contrast to AMSR2 and iQuam, MWRI displays significantly higher ESD and lower $SNR_{SUb}$. Abnormal fluctuations in ESD and $SNR_{SUb}$ commence in February 2021, suggesting issues with MWRI sensor calibration or data processing. Resolution of this problem occurs by July 2022, with subsequent recovery of ESD and $SNR_{SUb}$.

Compared to iQuam SST, the bias in AMSR2 SST shows slight fluctuations around 0 °C, while the RMSE remains close to 0.5 °C. In contrast, both the bias and RMSE of MWRI SST exhibit larger and less regular fluctuations. From April 2019 to July 2022, the biases of MWRI SST during daytime and nighttime vary between −0.6 °C and 0.9 °C and between −1.25 °C and 0.8 °C, respectively. Similarly, the RMSE of MWRI SST during daytime and nighttime fluctuates between 1.1 °C and 1.6 °C and between 1.1 °C and 1.7 °C, respectively, over the same period. Since July 2022, the biases of MWRI SST during both daytime and nighttime have been constrained within the range of −0.5 °C to 0.25 °C, with the RMSE reduced to below 1.2 °C. Considering the variations in ESD, $SNR_{SUb}$, bias and RMSE, it can be concluded that the performance of MWRI has improved following the resolution of sensor calibration or data processing issues since July 2022.

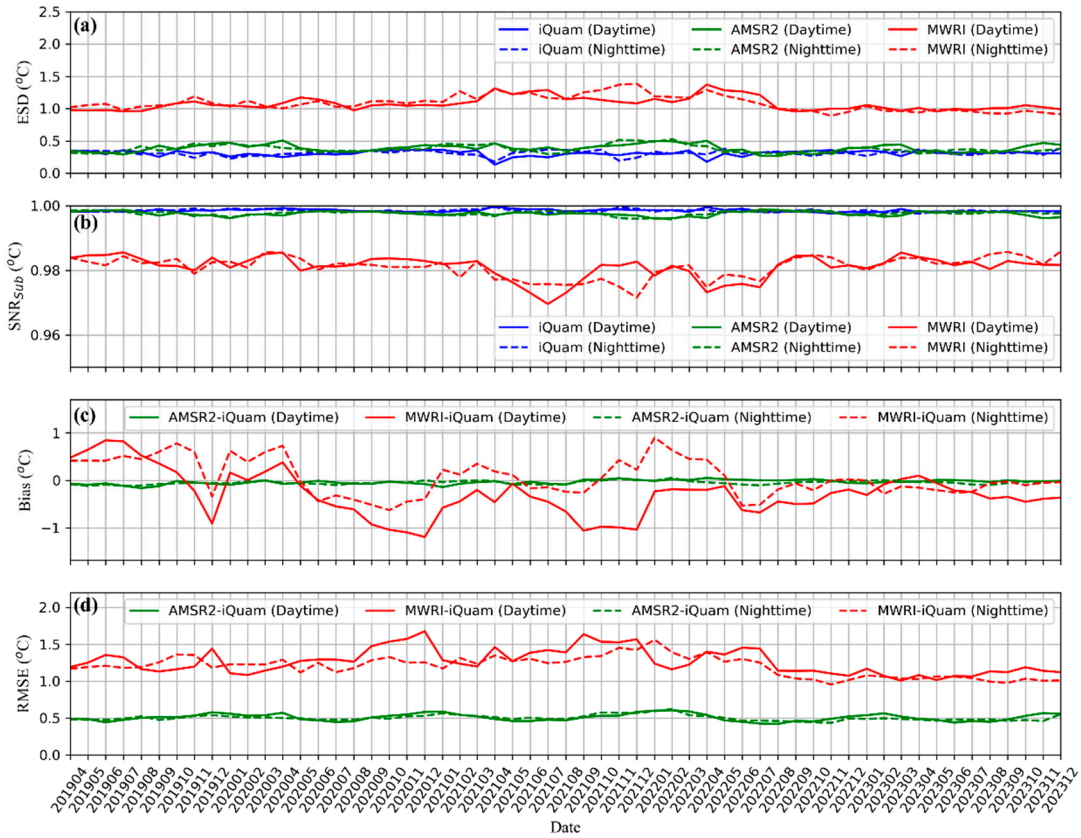


**Figure 6.** Temporal variation in error characteristics. (**a**) ESD. (**b**) $SNR_{SUb}$. (**c**) Bias. (**d**) RMSE.

(b) Latitudinal variation in error characteristics

Figure 7 exhibits how SST error characteristics of iQuam, AMSR2, and MWRI changing with latitude. All the SST error characteristics of iQuam, AMSR2, and MWRI exhibit clear latitudinal variations. The curves of ESD and $SNR_{SUb}$ for iQuam, AMSR2, and MWRI during both daytime and nighttime nearly overlap, making it difficult to distinguish performance differences between daytime and nighttime. The ESDs of all three measurement systems show similar variation patterns with latitude, increasing as latitude increases. However, MWRI exhibits significantly higher ESD values compared to the other two sys-

tems. iQuam and AMSR2 have similar ESD values in the latitude range of 62°S to 50°N, with AMSR2's ESD surpassing that of iQuam for latitudes greater than 50°N. In the latitude range of 0° to 20°N, all three measurement systems exhibit relatively low random error. However, low $SNR_{SUb}$ values indicate poor performance in detecting SST variation within this latitude range, especially around 10°N where the SST variation is relatively weak. For latitudes greater than 50°N and 50°S, $SNR_{SUb}$ values for all three measurement systems decrease as latitude increases due to synchronous increases in random error. In areas with high latitudes, sea surface wind speeds tend to increase, particularly in the Southern Hemisphere, which can have a negative impact on SST retrievals.

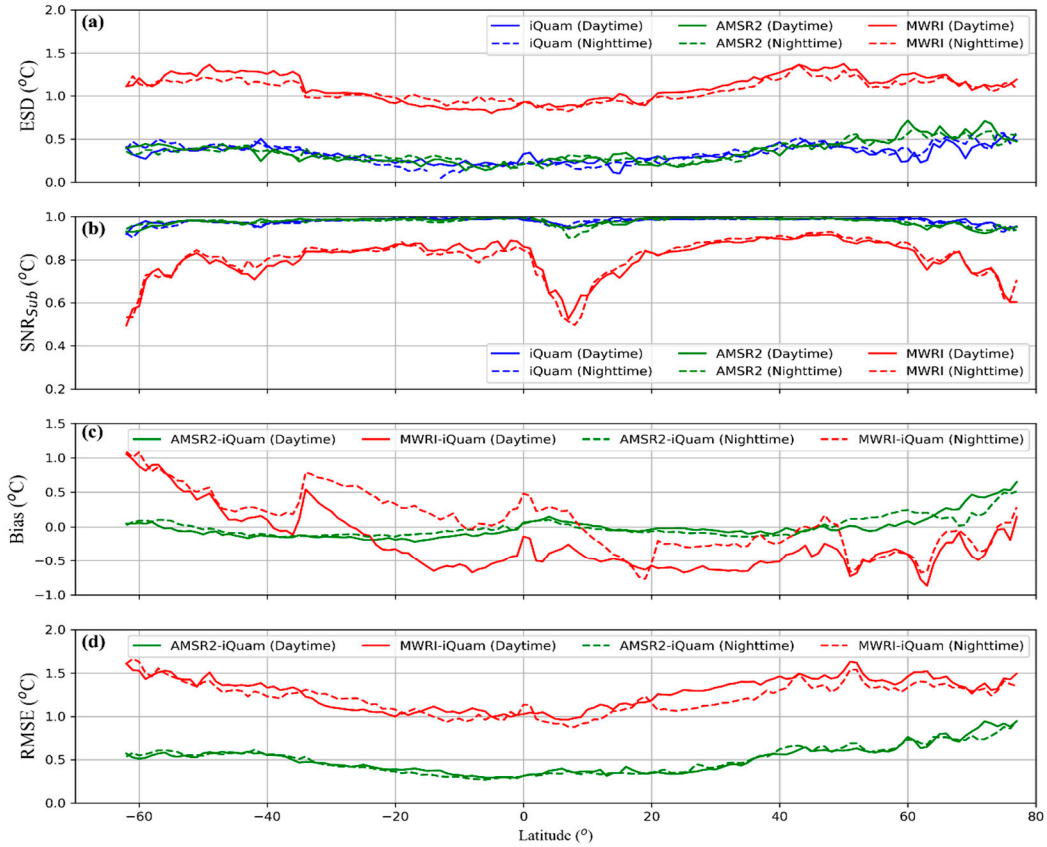


**Figure 7.** Latitudinal variation in error characteristics. (**a**) ESD. (**b**) $SNR_{SUb}$. (**c**) Bias. (**d**) RMSE.

As illustrated in Figure 7c, the bias of AMSR2 SST compared with iQuam SST ranges between −0.2 °C and 0.2 °C in the latitude range of 62°S to 50°N. Beyond 50°N, the bias of AMSR2 SST increases with latitude, peaking at 0.65 °C around 77°N. The RMSE of AMSR2 SST varies between 0.5 °C and 0.6 °C in the latitude range of 62°S to 35°S, decreasing to below 0.5 °C in the latitude range of 35°S to 35°N. From 35°N to 77°N, the RMSE of AMSR2 SST monotonically increases with latitude, reaching a maximum of 0.95 °C. The bias of MWRI SST compared with iQuam SST exhibits irregular fluctuations ranging from −0.8 °C to 1.1 °C, with the maximum occurring around 62°S. During daytime, MWRI SST shows warm biases for latitudes greater than 40°S in the Southern Hemisphere and negative biases in the latitude range of 26°S to 72°N. Conversely, during nighttime, the curve of the bias of MWRI SST mostly lies above the zero-bias line from 62°S to 7°N, indicating a warm bias across most of the Southern Hemisphere. However, from 7°N to 72°N, the curve of the bias of MWRI SST during nighttime mostly lies below the zero-bias line, indicating a negative bias across most of the Northern Hemisphere. This corresponds to the findings depicted in Figure 5. The RMSE of MWRI SST increases with latitude, exhibiting a minimum value of about 0.92 °C around 6°N and a maximum value of about 1.67 °C around 62°N. For MWRI, both the bias and the RMSE show significant jumps around 35°S, 0°, 18°N, and 52°N.

(c) Variation in error characteristics relate to SST

Error characteristics are depicted in Figure 8 within 2 °C SST intervals ranging from −3 °C to 34 °C. The ESD of iQuam decreases with increasing SST. AMSR2 exhibits increasing ESD from −3 °C to 8 °C and decreasing thereafter. MWRI's ESD exhibits a similar pattern with a higher magnitude, peaking around 10 °C. The $SNR_{SUb}$ of iQuam, AMSR2, and MWRI exhibit similar variations with SST. Within the SST range of 2 °C to 27 °C, $SNR_{SUb}$ slightly increases with rising SST, whereas it exhibits a rapid decline as SST decreases from 2 °C to −3 °C, and increases from 27 °C to 34 °C. The variations in ESD and $SNR_{SUb}$ with respect to SST align with the latitudinal variation findings; low latitudes correspond to high SST, while high latitudes correspond to low SST.

Illustrated in Figure 8c,d, the bias of AMSR2 SST relative to iQuam SST decreases from 0.4 °C to 0 °C within the SST range of −3 °C to 10 °C, whereas the RMSE exhibits a monotonic decline with increasing SST. Between SSTs of −3 °C and 5 °C, both daytime and nighttime biases of MWRI SST decline sharply. Within the SST range of 5 °C to 34 °C, MWRI SST exhibits a negative bias during the daytime, while nighttime bias varies around 0 °C. Similarly to AMSR2 SST, the RMSE of MWRI SST decreases monotonically with increasing SST, both during the daytime and nighttime, albeit with the daytime RMSE being smaller. Compared to AMSR2 SST, the bias and RMSE of MWRI SST exhibit more significant accuracy variations for SSTs below 5 °C. This is because MWRI has a lowest working frequency of 10.7 GHz, while AMSR2 has a lowest working frequency of 6.925 GHz. As concluded by Gentemann et al. (2010), 11 GHz SST retrievals are less accurate than 7 GHz retrievals, particularly in colder water [56].

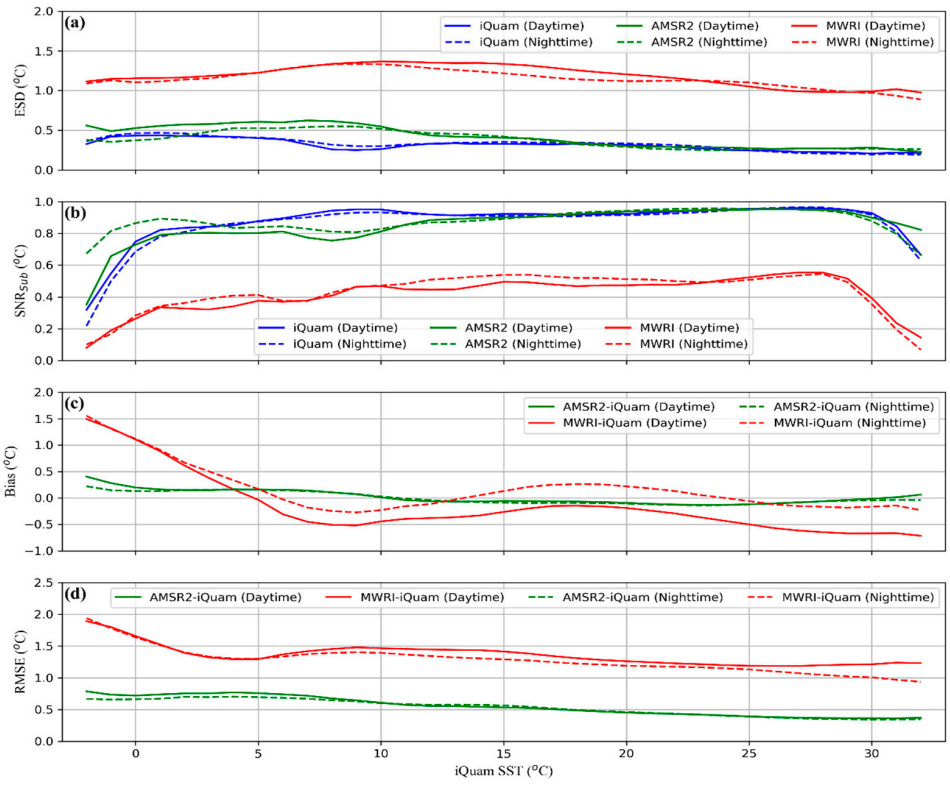


**Figure 8.** Variation in error characteristics along SST. (**a**) ESD. (**b**) $SNR_{SUb}$. (**c**) Bias. (**d**) RMSE.

(d) Variation in error characteristics relate to sea surface wind

Sea surface wind speed is an important environmental parameter that affects the accuracy of SST measurements. High sea surface wind speeds increase ocean water mixing, thereby reducing temperature differences between different depths. Additionally, whitecaps appear in association with high sea surface wind speeds, increasing the uncertainty of

SST retrievals. Figure 9 illustrates the changes in error characteristics with sea surface wind speed in 1 m/s intervals. Due to the limited number of triple collocations for sea surface wind speeds higher than 15 m/s, the variation in error characteristics related to sea surface wind is analyzed within the range of 0 m/s to 15 m/s.

The ESD of AMSR and MWRI exhibits a similar relationship with sea surface wind speed. Fluctuations are minimal when the sea surface wind speed is less than 9 m/s. However, when the wind speed exceeds 9 m/s, the ESD increases with increasing sea surface wind speed. Furthermore, the ESD of AMSR2 and MWRI is higher during the daytime than at nighttime. The $SNR_{SUb}$ of AMSR2 and MWRI tends to decrease when the wind speed exceeds 9 m/s, with daytime values being lower than nighttime values. This suggests that the performance of AMSR2 and MWRI during the daytime is inferior to that during the nighttime. In contrast to AMSR2 and MWRI, the iQuam ESD decreases with increasing wind speed when it exceeds 9 m/s. This occurs because the mixing of seawater at high wind speeds reduces the difference between the subsurface temperature and the skin temperature, thereby making the iQuam SST closer to the true SST value.

Compared to iQuam SST, the bias of AMSR2 SST exhibits slight oscillations near zero when the sea surface wind speed exceeds 5 m/s. However, the absolute bias increases as the wind speed decreases below 5 m/s. The RMSE of AMSR2 SST is minimized at a wind speed of 4.5 m/s, approximately 0.38 °C. The RMSE of AMSR2 SST increases as the wind speed deviates from 4.5 m/s, reaching its maximum of 0.84 °C at a wind speed of 15 m/s. For MWRI SST, the bias is negative during nighttime when the sea surface wind speed is less than 10 m/s. Positive bias occurs during the daytime when the wind speed is less than 4.5 m/s or greater than 8 m/s. The RMSE of MWRI SST is relatively large at low and high wind speeds, but smaller at moderate wind speeds. The minimum RMSE for MWRI SST occurs at a wind speed of 8.5 m/s, approximately 1.23 °C, during the daytime, and at a wind speed of 4.5 m/s, approximately 1.15 °C, during nighttime. During daytime, the RMSE of MWRI SST is lower than that of nighttime when the wind speed exceeds 2 m/s.

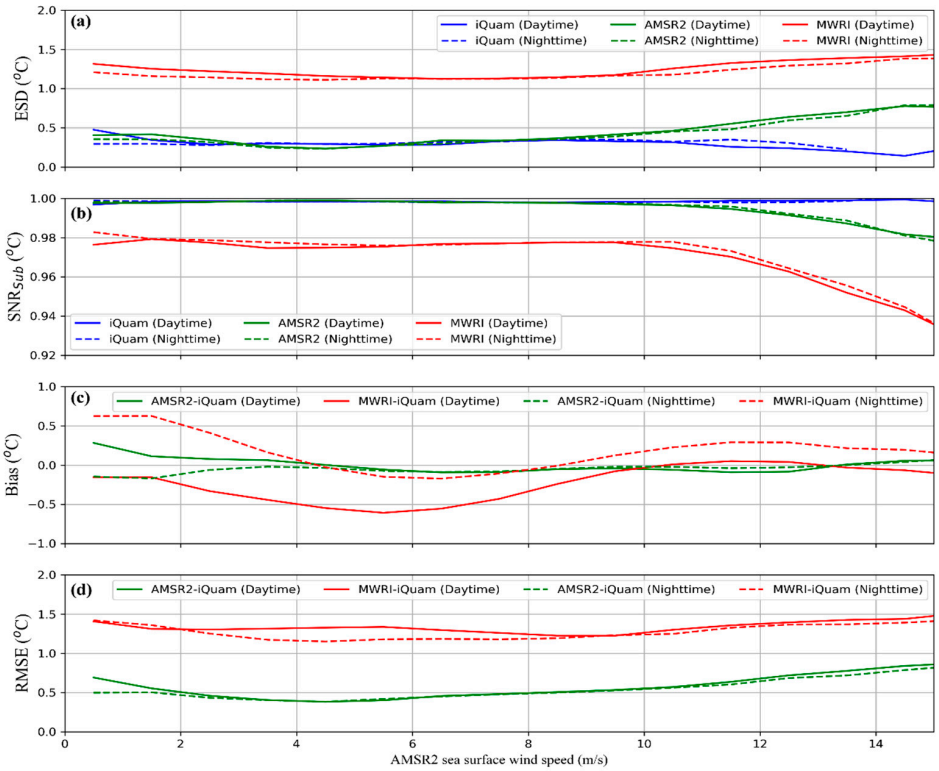


**Figure 9.** Variation in error characteristics along sea surface wind speed. (**a**) ESD. (**b**) $SNR_{SUb}$. (**c**) Bias. (**d**) RMSE.

(e) Variation in error characteristics relate to columnar water vapor

The attenuation and radiation of water vapor in the atmosphere contribute to the signal received by spaceborne microwave radiometers, which increase the uncertainty of SST retrieval. Figure 10 illustrates the variation in error characteristics with columnar water vapor. iQuam SST is not included in the analyses in this section because columnar water vapor does not directly affect iQuam SST.

The ESD of AMSR2 decreases with increasing columnar water vapor within the range of 2 mm to 30 mm, stabilizing at approximately 0.3 °C thereafter. The $SNR_{SUb}$ of AMSR2 decreases as columnar water vapor decreases below 10 mm or increases above 40 mm. The bias of AMSR2 SST relative to iQuam SST is positive within the range of 3 mm to 11 mm of columnar water vapor, with a maximum bias of 0.2 °C. When columnar water vapor exceeds 12 mm, the bias of AMSR2 SST ranges from −0.13 °C to 0 °C, with slight fluctuations. For columnar water vapor less than 50 mm, the RMSE of AMSR2 SST decreases with increasing columnar water vapor, whereas it tends to increase when columnar water vapor exceeds 50 mm.

The ESD of MWRI increases with columnar water vapor when it is less than 8 mm, and decreases when it exceeds 8 mm. The $SNR_{SUb}$ of MWRI follows a similar trend as the ESD with columnar water vapor, peaking at 14 mm. Relative to iQuam SST, MWRI SST during the daytime exhibits a negative bias except for columnar water vapor less than 7 mm or greater than 59 mm, while nighttime bias is positive. The RMSE of MWRI SST decreases with columnar water vapor when it is less than 58 mm. However, in nighttime conditions, it tends to increase when columnar water vapor exceeds 58 mm. Furthermore, the RMSE of MWRI SST is lower during nighttime than during daytime, indicating higher accuracy at night.

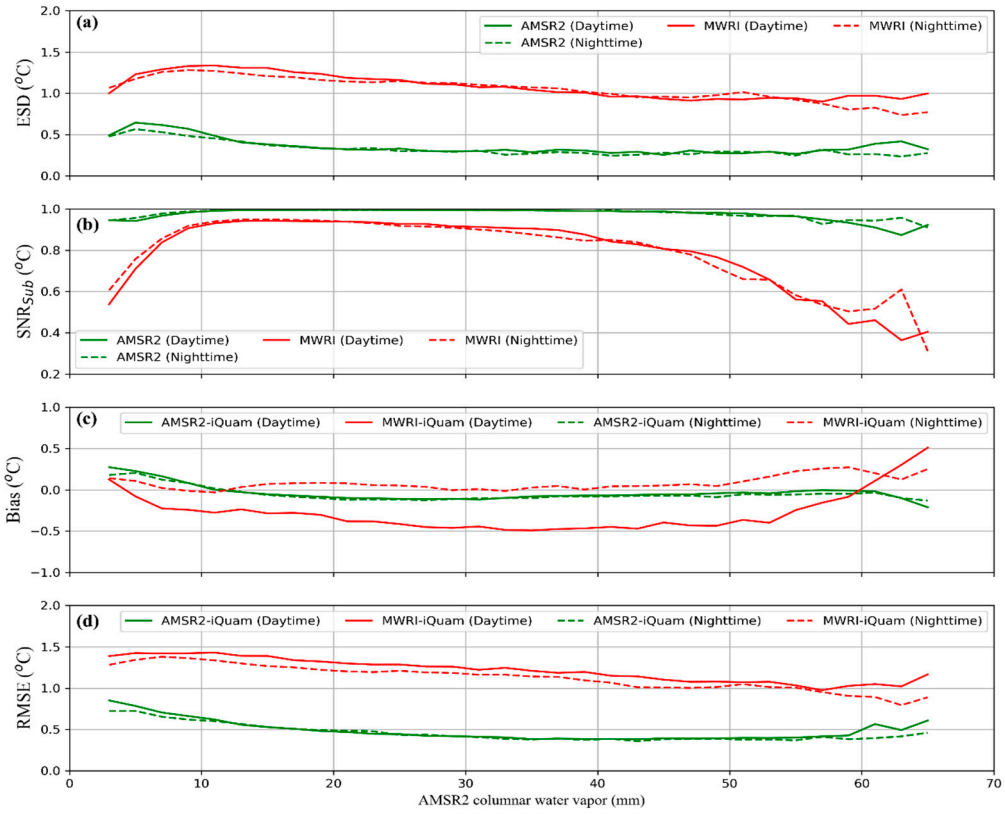


**Figure 10.** Variation in error characteristics along columnar water vapor. (**a**) ESD. (**b**) $SNR_{SUb}$. (**c**) Bias. (**d**) RMSE.

High columnar water vapor in the atmosphere results in high attenuation and radiation, which negatively affect SST retrieval from the brightness temperature received by

satellite-based microwave radiometers. Consequently, both the bias and RMSE of MWRI and AMSR2 increase with increasing columnar water vapor. For columnar water vapor below 10 mm, the bias and RMSE also increase because lower columnar water vapor commonly exists in areas with colder SST, where the accuracy of SST retrieval declines.

(f) Variation in error characteristics relate to columnar cloud liquid water

Like water vapor, the presence of liquid water in the atmosphere elevates the uncertainty of SST retrieval by spaceborne microwave radiometers. Figure 11 depicts the variation in error characteristics of AMSR2 and MWRI with columnar cloud liquid water.

With increasing columnar liquid water, the ESD of AMSR2 and MWRI tends to increase, while the $SNR_{SUb}$ tends to decrease. The ESD during nighttime is consistently lower than during the day, while the $SNR_{SUb}$ during nighttime is higher than that during the daytime. These differences become more pronounced with higher levels of columnar liquid water. The bias of AMSR2 SST relative to iQuam SST shows no obvious change with columnar liquid water, but the RMSE increases with increasing levels of columnar liquid water. The bias of MWRI SST during the daytime is consistently negative, with a mean value of −0.35 °C. However, during the nighttime, it ranges from −0.4 °C to 0.15 °C, with positive bias when columnar cloud liquid water is less than 0.1 mm and negative bias when it exceeds 0.1 mm. The lower ESD, higher $SNR_{SUb}$, and smaller RMSE during nighttime compared to daytime indicate that both AMSR2 and MWRI perform better at night.

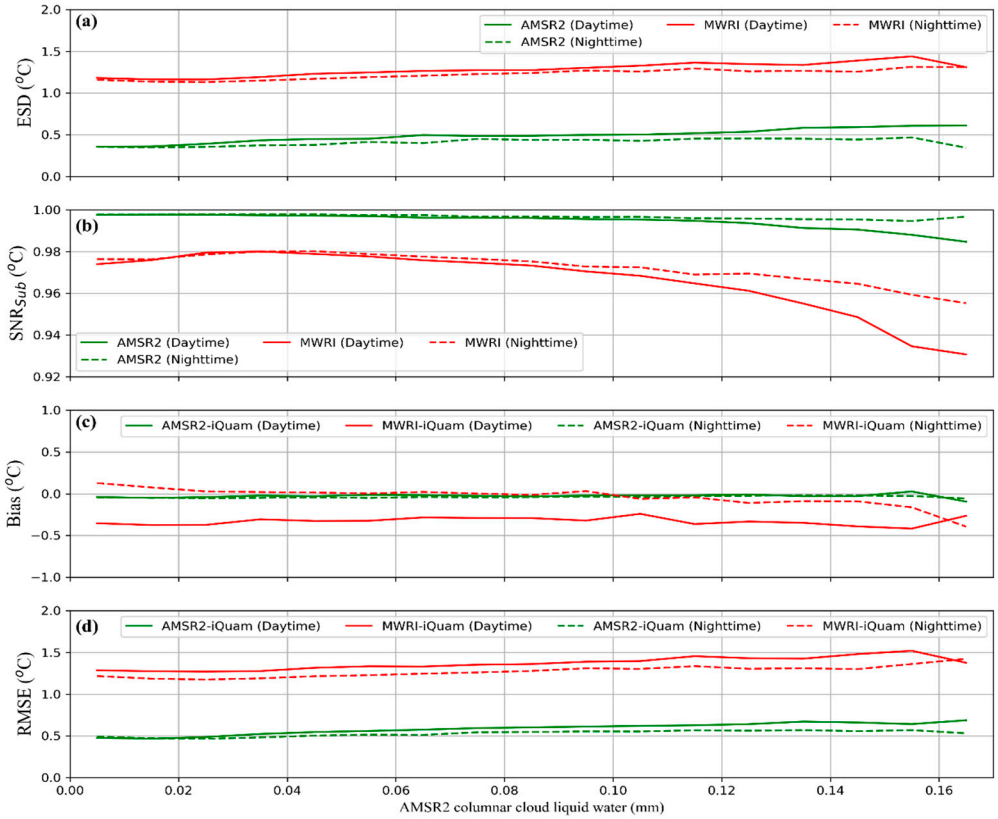


**Figure 11.** Variation in error characteristics along columnar cloud liquid water (**a**) ESD. (**b**) $SNR_{SUb}$. (**c**) Bias. (**d**) RMSE.

## 4. Discussion

The accuracy of sea surface temperature (SST) observations obtained from satellite-based infrared radiometers ranges from 0.3 to 0.6 °C [15–17], while those from microwave radiometers range from 0.4 to 0.6 °C [23–26]. Nevertheless, the results of ETC analyses indicate that the random error in in situ SST measurements falls within the range of 0.20 to 0.84 °C, a range consistent with previous findings [49]. Additionally, the random errors in

iQuam SST measurements exhibit variability dependent on the platform and location. Thus, employing iQuam SST measurements to validate SST observations from satellite-based infrared radiometers and microwave radiometers requires careful consideration of in situ SST selection. This study recommends the use of SST measurements from Drifters, T-M platforms, Argo, and HR-D platforms, which exhibit relatively lower random errors, for validating SST observations from satellite-based microwave radiometers. Conversely, SST measurements from ships, C-M platforms, and IMOS should be utilized cautiously.

The RSS AMSR2 SST product is generated based on well-calibrated brightness temperatures [26]. A significant enhancement in version 8.2 is the elimination of spurious drift in the AMSR2 SST, the version utilized in this study. The validation results demonstrate higher accuracy compared to version 7.2 of the SST product [26]. The SST observations from MWRI aboard FY-3D utilized in this study are operational products officially published by the National Satellite Meteorological Center. The validation results are consistent with those reported in [30], which validate the SST from MWRI aboard FY-3C. In a recent study, Li et al. (2024) endeavored to enhance the accuracy of FY-3D MWRI SST retrieval by incorporating pseudo-sea surface emissivity into the retrieval algorithm [57]. They achieved an SST retrieval with a RMSE of 1.10 °C and a bias of 0.12 °C. It can be inferred that the FY-3D MWRI SST has the potential for improvement.

Variations in SST magnitude across different locations can lead to inconsistencies between the abilities of various platforms to detect SST variations and their associated random errors or RMSE. For example, T-M platforms typically exhibit minimal random errors; however, their minimum $SNR_{SUb}$ suggests that this noise level may not be adequate for detecting fully tropical SST variations. Moreover, the $SNR_{SUb}$ introduced in ETC evaluates only the relative performance of SST variation detection, rather than providing information on the minimum detectable SST variation by the measurement system. This aspect warrants further investigation in future research.

## 5. Summary

SST is crucial for marine environmental studies and has significant implications for global climate and marine ecosystems. Validating remote-sensed SST products is a key step preceding their operational applications. In situ SST measurements collected by various platforms, utilizing different sensor types, and published by various organizations also need to be carefully evaluated and selected before specific applications. The focus is on intercomparing the in situ SST product of iQuam with the remotely sensed SST products from the spaceborne microwave radiometers AMSR2 and MWRI. The intercomparisons cover the period from 1 April 2019 to 31 December 2023, aiming to assess the quality of these SST products. Both ETC and direct comparison methods are employed in the intercomparison. In contrast to validation focused solely on SST measurement accuracy, this study also evaluates the capability to detect SST variations and assesses the random errors of the SST measurement systems.

While the iQuam SST product undergoes quality control, ETC analysis results demonstrate that the quality of SSTs varies among different platforms. Ships exhibit the highest random error, exceeding 0.83 °C, while T-M platforms demonstrate the minimum random error, below 0.28 °C. Drifters and HR-D platforms exhibit equal random errors since they belong to the same platform type. The total ESD and $SNR_{SUb}$ of AMSR2 are about 0.42 °C and 0.9974, respectively, which are similar to those of iQuam. MWRI exhibits a total ESD approximately 1.20 °C and a total $SNR_{SUb}$ around 0.9782. In comparison to iQuam and AMSR2, MWRI demonstrates a higher total ESD and a lower $SNR_{SUb}$, indicating higher random error and weaker capability for detecting SST variations. The bias and RMSE of AMSR2 and MWRI are examined through direct comparison using SST measurements from Drifters, T-M platforms, Argo floats, and HR-D platforms as the ground truth. The RMSE of AMSR2 SST is approximately 0.51 °C, with a bias of −0.05 °C. The RMSE of MWRI SST is approximately 1.26 °C, with a bias of −0.14 °C, consistent with [30]. The RMSE of AMSR2

SST and MWRI SST is lower during the daytime compared to nighttime. The biases of AMSR2 and MWRI exhibit obvious spatial variations.

Further analysis reveals the good temporal stability of iQuam and AMSR2 SSTs. MWRI experienced issues with sensor calibration or data processing between February 2021 and July 2022. The bias and RMSE of MWRI SST decreased after the problem was resolved. In the latitude range of 0° to 20°N, as well as for latitudes greater than 50°N and 50°S, the SST variation detection capability of iQuam, AMSR2, and MWRI significantly declines. For sea surface wind speeds exceeding 9 m/s, the random error of iQuam declines with increasing wind speed. However, the random errors and RMSE of AMSR2 and MWRI tend to increase, resulting in a decline in $SNR_{SUb}$. Compared with AMSR2 SST, the error characteristics of MWRI SST exhibit significant variations related to columnar water vapor, indicating that MWRI SST suffers from the crosstalk effect of columnar water vapor. Additionally, the error characteristics of AMSR2 SST and MWRI SST show a similar relationship with columnar cloud liquid water. As columnar cloud liquid water increases, the ESD and RMSE increase, while $SNR_{SUb}$ declines.

**Author Contributions:** Conceptualization, Y.Z.; methodology, Y.Z. and W.Z.; code, validation, and analysis, Y.Z., W.Z. and P.L.; writing—original draft preparation, Y.Z. and P.L.; writing—review and editing, Y.Z. and W.Z. All authors have read and agreed to the published version of the manuscript.

**Funding:** This study was funded by the National Natural Science Foundation of China, grant number 42376181.

**Data Availability Statement:** All the datasets used in this study are publicly available. The data sources are as follows: (1) Level 2 orbital SST product from MWRI/FY-3D, available at https://satellite.nsmc.org.cn (accessed on 28 February 2024). (2) SST product of AMSR2/GCOM-W1, available at https://data.remss.com (accessed on 28 February 2024). (3) In situ SST Quality Monitor (iQuam) SST, available at https://www.star.nesdis.noaa.gov/socd/sst/iquam/ (accessed on 28 February 2024).

**Acknowledgments:** We would like to thank the National Satellite Meteorological Center (NSMC), Remote Sensing System (RSS), and National Oceanic and Atmospheric Administration (NOAA) for providing the data used in this study.

**Conflicts of Interest:** The authors declare no conflicts of interest.

## References

1. Pisano, A.; Marullo, S.; Artale, V.; Falcini, F.; Yang, C.; Leonelli, F.E.; Santoleri, R.; Buongiorno Nardelli, B. New Evidence of Mediterranean Climate Change and Variability from Sea Surface Temperature Observations. *Remote Sens.* **2020**, *12*, 132. [CrossRef]
2. Ateweberhan, M.; McClanahan, T.R. Relationship between Historical Sea-Surface Temperature Variability and Climate Change-Induced Coral Mortality in the Western Indian Ocean. *Mar. Pollut. Bull.* **2010**, *60*, 964–970. [CrossRef] [PubMed]
3. Enfield, D.B.; Mestas-Nuñez, A.M. Multiscale Variabilities in Global Sea Surface Temperatures and Their Relationships with Tropospheric Climate Patterns. *J. Clim.* **1999**, *12*, 2719–2733. [CrossRef]
4. Ruela, R.; Sousa, M.C.; deCastro, M.; Dias, J.M. Global and Regional Evolution of Sea Surface Temperature under Climate Change. *Glob. Planet. Chang.* **2020**, *190*, 103190. [CrossRef]
5. O'Carroll, A.G.; Armstrong, E.M.; Beggs, H.M.; Bouali, M.; Casey, K.S.; Corlett, G.K.; Dash, P.; Donlon, C.J.; Gentemann, C.L.; Høyer, J.L.; et al. Observational Needs of Sea Surface Temperature. *Front. Mar. Sci.* **2019**, *6*, 420. [CrossRef]
6. Hausmann, U.; Czaja, A. The Observed Signature of Mesoscale Eddies in Sea Surface Temperature and the Associated Heat Transport. *Deep Sea Res. Part Oceanogr. Res. Pap.* **2012**, *70*, 60–72. [CrossRef]
7. Wang, Y.; Yu, Y.; Zhang, Y.; Zhang, H.-R.; Chai, F. Distribution and Variability of Sea Surface Temperature Fronts in the South China Sea. *Estuar. Coast. Shelf Sci.* **2020**, *240*, 106793. [CrossRef]
8. Tandeo, P.; Chapron, B.; Ba, S.; Autret, E.; Fablet, R. Segmentation of Mesoscale Ocean Surface Dynamics Using Satellite SST and SSH Observations. *IEEE Trans. Geosci. Remote Sens.* **2014**, *52*, 4227–4235. [CrossRef]
9. Fox-Kemper, B.; Adcroft, A.; Böning, C.W.; Chassignet, E.P.; Curchitser, E.; Danabasoglu, G.; Eden, C.; England, M.H.; Gerdes, R.; Greatbatch, R.J.; et al. Challenges and Prospects in Ocean Circulation Models. *Front. Mar. Sci.* **2019**, *6*, 65. [CrossRef]
10. Dong, B.; Dai, A.; Vuille, M.; Timm, O.E. Asymmetric Modulation of ENSO Teleconnections by the Interdecadal Pacific Oscillation. *J. Clim.* **2018**, *31*, 7337–7361. [CrossRef]
11. Jha, B.; Hu, Z.-Z.; Kumar, A. SST and ENSO Variability and Change Simulated in Historical Experiments of CMIP5 Models. *Clim. Dyn.* **2014**, *42*, 2113–2124. [CrossRef]

12. Kennedy, J.J. A Review of Uncertainty in in Situ Measurements and Data Sets of Sea Surface Temperature. *Rev. Geophys.* **2014**, *52*, 1–32. [CrossRef]
13. Xu, F.; Ignatov, A. In Situ SST Quality Monitor (iQuam). *J. Atmos. Ocean. Technol.* **2014**, *31*, 164–180. [CrossRef]
14. Minnett, P.J.; Alvera-Azcárate, A.; Chin, T.M.; Corlett, G.K.; Gentemann, C.L.; Karagali, I.; Li, X.; Marsouin, A.; Marullo, S.; Maturi, E.; et al. Half a Century of Satellite Remote Sensing of Sea-Surface Temperature. *Remote Sens. Environ.* **2019**, *233*, 111366. [CrossRef]
15. Minnett, P.J. The Validation of Sea Surface Temperature Retrievals from Spaceborne Infrared Radiometers. In *Oceanography from Space*; Barale, V., Gower, J.F.R., Alberotanza, L., Eds.; Springer: Dordrecht, The Netherlands, 2010; pp. 229–247. ISBN 978-90-481-8680-8.
16. Zhang, H.; Beggs, H.; Griffin, C.; Govekar, P.D. Validation of Himawari-8 Sea Surface Temperature Retrievals Using Infrared SST Autonomous Radiometer Measurements. *Remote Sens.* **2023**, *15*, 2841. [CrossRef]
17. Koutantou, K.; Brunner, P.; Vazquez-Cuervo, J. Validation of NASA Sea Surface Temperature Satellite Products Using Saildrone Data. *Remote Sens.* **2023**, *15*, 2277. [CrossRef]
18. Wentz, F.J.; Gentemann, C.; Smith, D.; Chelton, D. Satellite Measurements of Sea Surface Temperature Through Clouds. *Science* **2000**, *288*, 847–850. [CrossRef] [PubMed]
19. Gloersen, P.; Barath, F. A Scanning Multichannel Microwave Radiometer for Nimbus-G and SeaSat-A. *IEEE J. Ocean. Eng.* **1977**, *2*, 172–178. [CrossRef]
20. Bernstein, R.L. Sea Surface Temperature Mapping with the SEASAT Microwave Radiometer. *J. Geophys. Res. Oceans* **1982**, *87*, 7865–7872. [CrossRef]
21. Gentemann, C.L.; Wentz, F.J.; Mears, C.A.; Smith, D.K. In Situ Validation of Tropical Rainfall Measuring Mission Microwave Sea Surface Temperatures. *J. Geophys. Res. Oceans* **2004**, *109*, C04021. [CrossRef]
22. Stammer, D.; Wentz, F.; Gentemann, C. Validation of Microwave Sea Surface Temperature Measurements for Climate Purposes. *J. Clim.* **2003**, *16*, 73–87. [CrossRef]
23. Nielsen-Englyst, P.; Høyer, J.L.; Toudal Pedersen, L.; Gentemann, C.L.; Alerskans, E.; Block, T.; Donlon, C. Optimal Estimation of Sea Surface Temperature from AMSR-E. *Remote Sens.* **2018**, *10*, 229. [CrossRef]
24. Meissner, T.; Wentz, F. High Quality Sea Surface Temperature from the Windsat Radiometer: Algorithm and Validation. In Proceedings of the 2007 IEEE International Geoscience and Remote Sensing Symposium, Barcelona, Spain, 23–28 July 2007; IEEE: Barcelona, Spain, 2007; pp. 862–864.
25. Kim, H.-Y.; Park, K.-A.; Chung, S.-R.; Baek, S.-K.; Lee, B.-I.; Shin, I.-C.; Chung, C.-Y.; Kim, J.-G.; Jung, W.-C. Validation of Sea Surface Temperature (SST) from Satellite Passive Microwave Sensor (GPM/GMI) and Causes of SST Errors in the Northwest Pacific. *Korean J. Remote Sens.* **2018**, *34*, 1–15. [CrossRef]
26. Gentemann, C.L.; Hilburn, K.A. In Situ Validation of Sea Surface Temperatures from the GCOM-W 1 AMSR 2 RSS Calibrated Brightness Temperatures. *J. Geophys. Res. Oceans* **2015**, *120*, 3567–3585. [CrossRef]
27. Zhao, Y.; Zhu, J.; Lin, M.; Chen, C.; Huang, X.; Wang, H.; Zhang, Y.; Peng, H. Assessment of the Initial Sea Surface Temperature Product of the Scanning Microwave Radiometer Aboard on HY-2 Satellite. *Acta Oceanol. Sin.* **2014**, *33*, 109–113. [CrossRef]
28. Liu, M.; Guan, L.; Zhao, W.; Chen, G. Evaluation of Sea Surface Temperature From the HY-2 Scanning Microwave Radiometer. *IEEE Trans. Geosci. Remote Sens.* **2017**, *55*, 1372–1380. [CrossRef]
29. Zhang, L.; Yu, H.; Wang, Z.; Yin, X.; Yang, L.; Du, H.; Li, B.; Wang, Y.; Zhou, W. Evaluation of the Initial Sea Surface Temperature From the HY-2B Scanning Microwave Radiometer. *IEEE Geosci. Remote Sens. Lett.* **2021**, *18*, 137–141. [CrossRef]
30. Zhang, M.; Wang, S.; Qin, D.; Qiu, H.; Tang, S. The inversion and quality validation of FY-3C MWRI sea surface temperature. *Natl. Remote Sens. Bull.* **2018**, *22*, 713–722. [CrossRef]
31. Yang, Z.; Zhang, P.; Gu, S.; Hu, X.; Tang, S.; Yang, L.; Xu, N.; Zhen, Z.; Wang, L.; Wu, Q.; et al. Capability of Fengyun-3D Satellite in Earth System Observation. *J. Meteorol. Res.* **2019**, *33*, 1113–1130. [CrossRef]
32. Okuyama, A.; Imaoka, K. Intercalibration of Advanced Microwave Scanning Radiometer-2 (AMSR2) Brightness Temperature. *IEEE Trans. Geosci. Remote Sens.* **2015**, *53*, 4568–4577. [CrossRef]
33. Zhang, H.; Ignatov, A.; Hinshaw, D. Evaluation of the In Situ Sea Surface Temperature Quality Control in the NOAA in Situ SST Quality Monitor (iQuam) System. *J. Atmos. Ocean. Technol.* **2021**, *38*, 1249–1263. [CrossRef]
34. Woo, H.-J.; Park, K.-A. Inter-Comparisons of Daily Sea Surface Temperatures and In-Situ Temperatures in the Coastal Regions. *Remote Sens.* **2020**, *12*, 1592. [CrossRef]
35. Kennedy, J.J.; Rayner, N.A.; Smith, R.O.; Parker, D.E.; Saunby, M. Reassessing Biases and Other Uncertainties in Sea Surface Temperature Observations Measured in Situ since 1850: 1. Measurement and Sampling Uncertainties. *J. Geophys. Res. Atmos.* **2011**, *116*, D14103. [CrossRef]
36. Dong, S.; Gille, S.T.; Sprintall, J.; Gentemann, C. Validation of the Advanced Microwave Scanning Radiometer for the Earth Observing System (AMSR-E) Sea Surface Temperature in the Southern Ocean. *J. Geophys. Res. Oceans* **2006**, *111*, C04002. [CrossRef]
37. Donlon, C.J.; Minnett, P.J.; Gentemann, C.; Nightingale, T.J.; Barton, I.J.; Ward, B.; Murray, M.J. Toward Improved Validation of Satellite Sea Surface Skin Temperature Measurements for Climate Research. *J. Clim.* **2002**, *15*, 353–369. [CrossRef]
38. Minnett, P.J. Radiometric Measurements of the Sea-Surface Skin Temperature: The Competing Roles of the Diurnal Thermocline and the Cool Skin. *Int. J. Remote Sens.* **2003**, *24*, 5033–5047. [CrossRef]

39. Fairall, C.W.; Bradley, E.F.; Godfrey, J.S.; Wick, G.A.; Edson, J.B.; Young, G.S. Cool-Skin and Warm-Layer Effects on Sea Surface Temperature. *J. Geophys. Res. Oceans* **1996**, *101*, 1295–1308. [CrossRef]
40. Liu, Z.; Yang, M.; Qu, L.; Guan, L. Regional Study on the Oceanic Cool Skin and Diurnal Warming Effects: Observing and Modeling. *Remote Sens.* **2023**, *15*, 3814. [CrossRef]
41. Stoffelen, A. Toward the True Near-Surface Wind Speed: Error Modeling and Calibration Using Triple Collocation. *J. Geophys. Res. Oceans* **1998**, *103*, 7755–7766. [CrossRef]
42. Gruber, A.; Su, C.-H.; Zwieback, S.; Crow, W.; Dorigo, W.; Wagner, W. Recent Advances in (Soil Moisture) Triple Collocation Analysis. *Adv. Valid. Appl. Remote. Sensed Soil Moisture Part 1* **2016**, *45*, 200–211. [CrossRef]
43. Draper, C.; Reichle, R.; de Jeu, R.; Naeimi, V.; Parinussa, R.; Wagner, W. Estimating Root Mean Square Errors in Remotely Sensed Soil Moisture over Continental Scale Domains. *Remote Sens. Environ.* **2013**, *137*, 288–298. [CrossRef]
44. Peng, J.; Misra, S.; Piepmeier, J.R.; Dinnat, E.P.; Yueh, S.H.; Meissner, T.; Vine, D.M.L.; Shelton, K.E.; Freedman, A.P.; Dunbar, R.S.; et al. Soil Moisture Active/Passive (SMAP) L-Band Microwave Radiometer Post-Launch Calibration Upgrade. *IEEE J. Sel. Top. Appl. Earth Obs. Remote Sens.* **2019**, *12*, 1647–1657. [CrossRef]
45. Hong, Z.; Moreno, H.A.; Li, Z.; Li, S.; Greene, J.S.; Hong, Y.; Alvarez, L.V. Triple Collocation of Ground-, Satellite- and Land Surface Model-Based Surface Soil Moisture Products in Oklahoma—Part I: Individual Product Assessment. *Remote Sens.* **2022**, *14*, 5641. [CrossRef]
46. Li, C.; Tang, G.; Hong, Y. Cross-Evaluation of Ground-Based, Multi-Satellite and Reanalysis Precipitation Products: Applicability of the Triple Collocation Method across Mainland China. *J. Hydrol.* **2018**, *562*, 71–83. [CrossRef]
47. Wild, A.; Chua, Z.-W.; Kuleshov, Y. Triple Collocation Analysis of Satellite Precipitation Estimates over Australia. *Remote Sens.* **2022**, *14*, 2724. [CrossRef]
48. Hoareau, N.; Portabella, M.; Lin, W.; Ballabrera-Poy, J.; Turiel, A. Error Characterization of Sea Surface Salinity Products Using Triple Collocation Analysis. *IEEE Trans. Geosci. Remote Sens.* **2018**, *56*, 5160–5168. [CrossRef]
49. Xu, F.; Ignatov, A. Error Characterization in iQuam SSTs Using Triple Collocations with Satellite Measurements. *Geophys. Res. Lett.* **2016**, *43*, 10826–10834. [CrossRef]
50. Caires, S.; Sterl, A. Validation of Ocean Wind and Wave Data Using Triple Collocation. *J. Geophys. Res. Oceans* **2003**, *108*, 3098. [CrossRef]
51. McColl, K.A.; Vogelzang, J.; Konings, A.G.; Entekhabi, D.; Piles, M.; Stoffelen, A. Extended Triple Collocation: Estimating Errors and Correlation Coefficients with Respect to an Unknown Target. *Geophys. Res. Lett.* **2014**, *41*, 6229–6236. [CrossRef]
52. Entekhabi, D.; Reichle, R.H.; Koster, R.D.; Crow, W.T. Performance Metrics for Soil Moisture Retrievals and Application Requirements. *J. Hydrometeorol.* **2010**, *11*, 832–840. [CrossRef]
53. Zwieback, S.; Scipal, K.; Dorigo, W.; Wagner, W. Structural and Statistical Properties of the Collocation Technique for Error Characterization. *Nonlinear Process. Geophys.* **2012**, *19*, 69–80. [CrossRef]
54. Alerskans, E.; Høyer, J.L.; Gentemann, C.L.; Pedersen, L.T.; Nielsen-Englyst, P.; Donlon, C. Construction of a Climate Data Record of Sea Surface Temperature from Passive Microwave Measurements. *Remote Sens. Environ.* **2020**, *236*, 111485. [CrossRef]
55. Zhou, W.; Lin, M.; Li, W.; Yin, X.; Li, Y.; Li, X.; Li, Q.; Wang, S.; Yu, R. HY-2B SMR's Sea Surface Temperature Retrieval Considering Parameter Crosstalk. *IEEE Trans. Geosci. Remote Sens.* **2023**, *61*, 4207812. [CrossRef]
56. Gentemann, C.L.; Meissner, T.; Wentz, F.J. Accuracy of Satellite Sea Surface Temperatures at 7 and 11 GHz. *IEEE Trans. Geosci. Remote Sens.* **2010**, *48*, 1009–1018. [CrossRef]
57. Li, Z.C.; Jiang, G.M. Sea Surface Temperature Retrieval From the FY-3D MWRI Measurements. *IEEE Trans. Geosci. Remote Sens.* **2024**, *62*, 4201010. [CrossRef]


**Disclaimer/Publisher's Note:** The statements, opinions and data contained in all publications are solely those of the individual author(s) and contributor(s) and not of MDPI and/or the editor(s). MDPI and/or the editor(s) disclaim responsibility for any injury to people or property resulting from any ideas, methods, instructions or products referred to in the content.